

Radio-Near Infrared Imaging of Dual Active Galactic Nuclei Candidates

MAKOTO A. JOHNSTONE ,¹ ILSANG YOON ,^{2,1} EMMANUEL MOMJIAN ,³ LORETO BARCOS-MUNOZ ,^{2,1}
 A.S. EVANS ,^{1,2} BJORN EMONTS ,² EILAT GLIKMAN ,⁴ DONG-CHAN KIM ,² JI HOON KIM ,⁵ MINJIN KIM ,⁶
 MARK LACY ,² GEORGE C. PRIVON ,^{2,1,7} DEVAKY KUNNERIATH ,² JAYA NAGARAJAN-SWENSON ,¹
 NÚRIA TORRES-ALBÁ ,¹ AND KARA N. GREEN 

¹Department of Astronomy, University of Virginia, 530 McCormick Road, Charlottesville, VA 22903, USA

²National Radio Astronomy Observatory, 520 Edgemont Road, Charlottesville, VA 22903, USA

³National Radio Astronomy Observatory, P.O. Box O, Socorro, NM 87801, USA

⁴Department of Physics, Middlebury College, Middlebury, VT 05753, USA

⁵SNU Astronomy Research Center, Department of Physics and Astronomy, Seoul National University, 1 Gwanak-Ro, Gwanak-Gu, Seoul, 08826, Republic of Korea

⁶Department of Astronomy, Yonsei University, 50 Yonsei-ro, Seodaemun-gu, Seoul 03722, Republic of Korea

⁷Department of Astronomy, University of Florida, P.O. Box 112055, Gainesville, FL 32611, USA

ABSTRACT

We report the results of a pilot study that searched for dual active galactic nuclei (AGN) in local ($z < 0.25$) galaxies hosting double-peaked narrow emission lines in their optical spectra. We present high-resolution L –band (1.5 GHz or 18 cm) continuum images from the Very Long Baseline Array (VLBA) as well as WFC3/IR F160W images from the *Hubble Space Telescope* of two candidate dual AGN systems: J0948+6848 and J1223+5409. In both targets, we detected compact non-thermal radio emission that is approximately co-spatial with the near-infrared AGN. Both systems host two high brightness temperature ($> 10^8$ K) radio sources that indicate the presence of either a parsec-scale-separation dual AGN ($d_{\text{sep}} \sim 90$ pc and ~ 56 pc, respectively) or a radio jet. Matched-resolution multi-band radio observations are necessary to further characterize the AGN activity in these systems.

1. INTRODUCTION

Nearly all galaxies host a supermassive black hole (SMBH). During galaxy mergers, their central SMBHs lose energy and angular momentum via dynamical friction (Chandrasekhar 1943; Just et al. 2011), causing their nuclear separations to gradually decrease. Merger-driven inflows of gas and dust fuel accretion onto these SMBHs, triggering intense active galactic nucleus (AGN) activity (e.g., Hopkins et al. 2006). These merger-triggered AGN are responsible for the most extreme SMBH accretion events in the Universe (e.g., Treister et al. 2012; Glikman et al. 2015; Weigel et al. 2018; Euclid Collaboration et al. 2025).

Among the most significant episodes of AGN activity are those in which two (or more) SMBHs are simultaneously active within an interacting system (e.g., Van Wassenhove et al. 2012). At kiloparsec and subkiloparsec scale nuclear separations, these systems are referred to as dual AGNs (De Rosa et al. 2019; Pfeifle et al. 2025). Binary AGNs, in contrast, are gravitationally-bound Keplerian binaries that form after the merging galaxies have coalesced into a single common envelope (De Rosa et al. 2019; Pfeifle et al. 2025). These SMBH

binaries occur when nuclear separations have reached parsec to a few tens of parsec scales (depending on the SMBH mass and spin) and will continue to shrink via stellar hardening (e.g., Berczik et al. 2022), gas-driven inspirals (e.g., Rafikov 2016), and gravitational wave emission (e.g., Izquierdo-Villalba et al. 2022).

The recently detected stochastic gravitational wave (GW) background (e.g., Agazie et al. 2023a; Reardon et al. 2023; Xu et al. 2023) suggests that merging SMBHs are ubiquitous in the Universe (Agazie et al. 2023b). Empirical evidence of such a population, however, is limited. Despite extensive observational surveys at optical, infrared, and X-ray wavelengths (e.g., Koss et al. 2018; De Rosa et al. 2019), fewer than ten dual/binary AGNs with subkiloparsec-separations have been confirmed (e.g., Fabbiano et al. 2011; Kollatschny et al. 2020; Koss et al. 2023). In fact, only one binary AGNs showing two visible nuclei with < 100 pc projected nuclear separation has been detected thus far (0402+379; Rodriguez et al. 2006).

Insufficient spatial resolution and/or dust obscuration are among the factors that are likely responsible for this low detection rate. Specifically, resolving the dis-

tinct cores of close-separation AGN pairs often requires parsec-scale spatial resolutions that are only feasible in the local Universe. Furthermore, late-stage mergers, the most probable hosts of dual/binary AGN (Springel et al. 2005; Steinborn et al. 2016; Volonteri et al. 2016; De Rosa et al. 2019), tend to have heavy nuclear obscuration that can render the AGN non-detectable at most wavelengths (Ricci et al. 2017, 2021). Although radio continuum observations remain optically thin up to $N_H \sim 10^{26} \text{ cm}^{-2}$ (Hildebrand 1983), only $\sim 10\%$ of AGN are radio-loud (Urry & Padovani 1995; Burke-Spolaor 2011; Kellermann et al. 2016). Hence, even extinction-free radio observations would ‘miss’ a significant fraction of AGN in the Universe if not complemented by observations at another wavelength.

The possibility of false positives in some dual AGN diagnostics further complicates these observational searches. For example, while double-peaked narrow emission lines can be a signature of dual/binary AGNs (e.g., Smith et al. 2010), such spectroscopic features are more likely to be tracing gas outflows or rotational motions in the narrow line region (Fu et al. 2012). Similarly, astrometric variability in known AGN could indicate the presence of a hidden close-separation AGN binary (e.g., Hwang et al. 2020), but lensed quasar systems (e.g., Mannucci et al. 2022; Ciurlo et al. 2023), photometric fluctuations due to changes in obscuration, and astrometric errors due to extended host galaxies (Hwang et al. 2020) could create similar effects, thus requiring high resolution follow-up observations to confirm dual AGN presence (e.g., Chen et al. 2023). These limitations of single-band observations have emphasized the need for multi-wavelength studies for dual/binary AGN to both maximize the likelihood of detection and provide robust confirmation of an AGN pair. Indeed, several multi-wavelength studies over the last decade have generated robust dual/binary AGN detections at both low redshift ($z \lesssim 0.1$; e.g., Müller-Sánchez et al. 2015; Koss et al. 2023; Trindade Falcão et al. 2024) and high redshift ($z \sim 2$; e.g., Glikman et al. 2023; Gross et al. 2025).

Among these multi-wavelength identification techniques are searches for positional offsets between radio AGN and optical AGN (e.g., Orosz & Frey 2013; Kim et al. 2019; Veres et al. 2021; Chen et al. 2023; Popkov et al. 2025; Schwartzman et al. 2025). Specifically, Kim et al. (2019) observed a dual AGN separated by 1.6 kpc (0.26'' at $z = 0.3504$) in the galaxy CXO J101527.2+625911. This AGN pair was identified based on the significant spatial offset between the optical AGN and the radio AGN core, indicating that the system must host two distinct AGN. As further

evidence, the [OIII] $\lambda 5007$ line emission of the galaxy was best modeled by two emission line components, a phenomenon that can occur when the system hosts two distinct narrow line regions (Kim et al. 2017). It is therefore believed that the system consists of an optically-detected radio-quiet AGN and a radio-detected optically-obsured AGN (otherwise known as a ‘radio-optical’ AGN pair). Chen et al. (2023) employed a similar method in a systematic study in which they examined 23 dual/binary AGN candidates and compared the coordinates of their Gaia optical positions and their parsec-scale radio AGN emission. They measured significant positional differences in three systems which they identified as candidate dual/binary AGNs with parsec-scale projected nuclear separations.

The work of Kim et al. (2019) and Chen et al. (2023) demonstrated that comparisons of radio and optical/near-infrared images could effectively identify dual AGN, even when obscuration is present. In this work, we apply the technique used in Kim et al. (2019) to two candidate dual AGN systems to search for AGN pairs. In Section 2, we describe the sample selection criteria, followed by the data description in Section 3. We present the radio and near-infrared (NIR) images in Section 4 and report the detected AGN positions at each wavelength. In Section 5, we discuss the AGN properties and their implications. We present our final conclusions in Section 6. We adopt a flat cosmology with $H_0 = 70 \text{ km s}^{-1} \text{ Mpc}^{-1}$, $\Omega_M = 0.3$, and $\Omega_\Lambda = 0.7$.

2. SAMPLE

We selected our targets from the complete sample of 1271 local ($z < 0.25$) Sloan Digital Sky Survey (SDSS) Data Release 7 (DR7) quasars (Schneider et al. 2010). Spectral decomposition by Kim et al. (2020) found that 77 systems in this parent sample had double-peaked [OIII] emission line profiles. These profiles returned lower reduced χ^2 values when modeled by two Gaussian components rather than a single component, even when a ‘blue-shifted’ broad-line component was included in the model fit (see Figure 1 in this work or Table 2 in Kim et al. 2020). Such double-peaked line profiles could be tracing a dual/binary AGN system, the rotational kinematics of a single NLR or the interactions of an AGN jet with the interstellar medium (Greene & Ho 2005; Shen et al. 2011; Müller-Sánchez et al. 2015; Rubinur et al. 2019). The inclusion of the broad-line component in the spectral decomposition, however, helped eliminate double-peaked profiles generated by gas outflows, increasing the likelihood of identifying true dual AGN hosts.

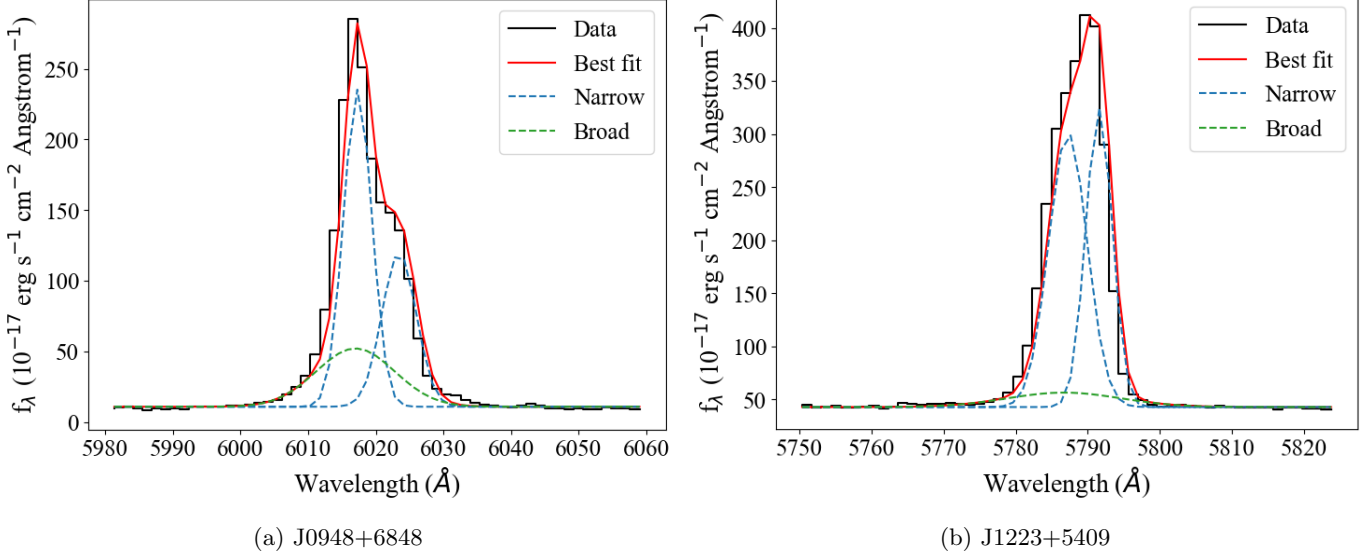


Figure 1. SDSS spectra showing the [OIII] λ 5007 lines of J0948+6848 (left) and J1223+5409 (right). The [OIII] line spectra are fitted best with the double narrow line components (blue) and one broad line component (green). Kim et al. (2020) identified these systems as candidate dual/binary AGN based on these double-peaked [OIII] line profiles.

Of the 77 dual/binary AGN candidates, Kim et al. (2020) found that 27 galaxies in this parent sample were detected at a > 0.72 mJy beam $^{-1}$ ($\gtrsim 6\sigma$ level, based on the 3σ contours in their Figure 14) by the first epoch of the Very Large Array Sky Survey (VLASS; Gordon et al. 2021; see Figure 14 in Kim et al. 2020), indicating the possible presence of at least one radio-bright AGN. We then required that the galaxies have Wide-field Infrared Survey Explorer (WISE) colors $W1-W2 > 0.5$ (Assef et al. 2013; Satyapal et al. 2014), which reduced the sub-sample to 26 galaxies. We applied this criterion to target galaxy mergers, given that both observations and radiative transfer simulations find that the mid-infrared color rises above this threshold just before the stage of peak black hole growth during galaxy mergers, an epoch during which dual AGN are most likely, making it an effective tool to search for merger-triggered AGN (e.g., Lacy et al. 2004; Satyapal et al. 2014) and dual AGN hosts (Satyapal et al. 2017; Blecha et al. 2018).

From this carefully selected sample, we target the two best galaxies, SDSS J094822.45+684835.2 ($z=0.202$) and SDSS J122313.21+540906.5 ($z=0.156$). These two systems had the brightest VLASS 3 GHz flux densities presented in Kim et al. (2020) (precise VLASS flux density measurements are presented in Section 5) and thus had the highest likelihood of hosting radio AGN. Hereafter, we refer to the targets as J0948+6848 and J1223+5409, respectively. In this work, we present the first targeted search for dual/binary AGN in these objects. At the redshifts of these galaxies, 1 mas corresponds to ~ 3 pc.

3. DATA DESCRIPTION

3.1. *HST* NIR Imaging

New *Hubble Space Telescope* (*HST*) images were obtained with the WFC3/IR F160W filter (central wavelength of $\lambda \sim 1.5 \mu\text{m}$) for both science targets (Program 16485, PI: I. Yoon). J0948+6848 and J1223+5409 were observed on August 27th, 2021 and May 16th, 2022, respectively. The observations were conducted across four identical iterations in a single orbit for a total exposure time of 2623 seconds per object. Data reduction and calibration were performed using the standard *HST* pipeline to produce Hubble Advance Products (HAP) Single Visit Mosaics (SVMs)². These SVM data products were Gaia-aligned (Gaia Collaboration et al. 2023) for improved astrometry and have a pixel-scale of $\sim 0.128''/\text{pixel}$. The *HST* data presented in this article were obtained from the Mikulski Archive for Space Telescopes (MAST) at the Space Telescope Science Institute. The specific observations analyzed can be accessed via doi: 10.17909/y3dt-km68.”

3.2. VLBA Continuum Imaging

We obtained high-resolution (~ 5 mas) *L*-band (1.5 GHz or 18 cm) continuum images using the Very Long Baseline Array (VLBA; Project BY157, PI: I. Yoon). We utilized the polyphase filterbank digital (PFB) system to deliver eight 32 MHz data channels,

² <https://archive.stsci.edu/contents/newsletters/december-2020/hap-single-visit-mosaics-now-available>

both with right- and left-hand circular polarizations. This corresponds to a total bandwidth of 256 MHz. The data were recorded at a rate of 2048 Mbit/s with 2-bit sampling. For both targets, we utilized phase-referencing with a three minute cycle time: two minutes on target and one minute on the calibrator. 4C39.25 was used as a fringe finder for both targets and to calibrate the bandpass response. The total on-target observing time was approximately 75 minutes using eight antennas for both science targets. The data were correlated with the DiFX software correlator (Deller et al. 2011) in Socorro, New Mexico, with a two-second integration time. The observation details are listed in Table 1.

The data reduction, calibration, and imaging of the data was conducted using the Astronomical Image Processing System (AIPS; Greisen 2003), following standard Very Long Baseline Interferometry procedures. Imaging of the phase calibrators confirmed that the emission was compact, allowing for precise phase-referencing calibrations. Self-calibration was performed on both targets to reduce phase and amplitude errors. Since the starting model is the post-phase-referencing model of the target, the additional astrometric uncertainty introduced by the self calibration is estimated to be a fraction of the synthesized beam and does not significantly impact the results presented in this work. The final VLBA continuum images were made with a robust factor of 0 in the AIPS task `IMAGR`, using the Clark Clean algorithm (Clark 1980). The 1σ root-mean-square noises of the continuum images are greater than the theoretical value of ($\sim 40\mu\text{m beam}^{-1}$) estimated by the European VLBI Network observation planner³ by factors of 1.1 and 1.4 for J0948+6848 and J1223+5409, respectively. We attribute this to significant data loss due to flagging of radio frequency interference ($\sim 40\%$ and $\sim 38\%$, respectively). The synthesized beam sizes and RMS noises of the continuum images are also provided in Table 1.

4. RESULTS

4.1. Modeling the NIR AGN position

Following the methodology of Kim et al. (2019), we modeled the host galaxy morphology and NIR AGN position of the *HST* F160W images using the two-dimensional fitting algorithm GALFIT (Peng et al. 2010). In our modeling procedure, we ensured that the fitting region was large enough to include the entire system and sufficient background sky ($0.77' \times 0.54'$ and $0.93' \times 0.68'$ regions for J0948+6848 and J1223+5409, respectively). We obtained an empirical point spread

function (PSF) by extracting images of all stars within the F160W image field of view (2 stars for J0948+6848, 3 stars for J1223+5409) and taking their median. We then modeled the host galaxy with a single PSF, a background sky component, and Sérsic component(s). Additional Sérsic components were added to account for neighboring galaxies that overlapped with the host galaxy. All other objects in the field of view were masked in order to reduce the χ^2_ν value of the model fit. In the final model, all variables were left as free parameters to ensure unbiased results.

Since J0948+6848 has a relatively symmetric structure, a single Sérsic component was sufficient to model the central host galaxy (Sérsic index $n \approx 1.66$; Figure 2). Since an exponential disk is defined as having a radial profile with a Sérsic index of $n = 1$, we interpret this as a disk-like galaxy with a slightly perturbed morphology. The galaxy morphology of J1223+5409, in contrast, is highly disturbed with several shell-like features and a tidal tail (Figure 3). We used four Sérsic components and employed the GALFIT Fourier and bending modes (Peng et al. 2010) in addition to the standard Sérsic parameters. Briefly, Fourier modes add perturbations onto a perfect ellipsoidal shape to create asymmetrical structures. The Fourier perturbations are defined as,

$$r(x, y) = r_0(x, y) \left(1 + \sum_{m=1}^N a_m \cos(m(\theta + \phi_m)) \right) \quad (1)$$

where $r_0(x, y)$ is the radial coordinate of a traditional ellipse, θ is the position angle, and a_m and ϕ_m are the Fourier amplitude and phase angle for mode m . Bending modes, in contrast, allow for curvature in the Sérsic components by perturbing a single axis, following the relation,

$$y' = y + \sum_{m=1}^N a_m \left(\frac{x}{R_{\text{eff}}} \right)^m \quad (2)$$

where (x, y) are the positions prior to the coordinate transformation, R_{eff} is the effective radius, and a_m is the amplitude for bending mode m . The addition of these features disentangled the asymmetric and/or distorted structures in J1223+5409 and significantly improved the model fit. We report the ‘best-fit’ GALFIT model parameters in Table 2 and present the model images in Figures 2 and 3.

We note that the original *HST* images had brightness units of electrons per second, but we modified the image to be in units of electrons for the GALFIT modeling. This allowed the program to generate correct sigma images to more estimate the χ^2_ν value, as explained in the

³ <https://planobs.jive.eu>

Table 1. Summary of VLBA L-band (1.5 GHz) observations

(1) Source	(2) Date	(3) Phase Calibrator	(4) Positional Accuracy (mas)	(5) Sep (deg)	(6) Beam (mas \times mas)	(7) P.A. (deg)	(8) 1 σ Noise (μ Jy beam $^{-1}$)
J0948+6848	Feb. 01, 2021	J0958+6533	0.03	3.40	11.5 \times 4.3	21.2	54
J1223+5409	Feb. 11, 2021	J1208+5441	0.18	2.15	11.6 \times 4.1	36.6	45

NOTE—Column (1): Source name. Column (2): Date of observations. Column (3): Phase calibrator. Column (4): Positional uncertainty of phase calibrator reported by the VLBA’s calibrator search tool^a. Column (5): The angular separation between the phase calibrator and the target in degrees. Column (6): Synthesized beam size of the continuum image. Column (7): Position angle of synthesized beam. Column (8): 1 σ RMS noise.

^a<https://obs.vlba.nrao.edu/cst/>

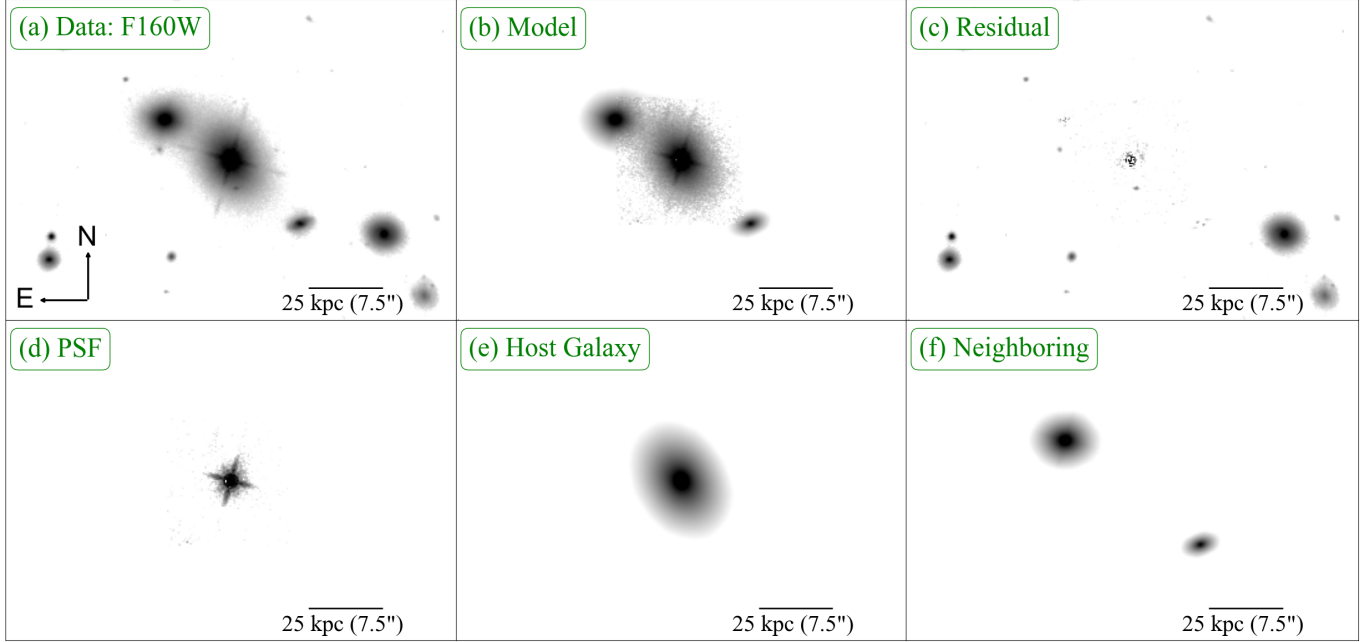
J0948+6848 ($\chi^2_\nu = 6.357$)

Figure 2. Best-fit GALFIT model of J0948+6848. Top row shows (a) the original image, (b) the model, and (c) the residual image. The bottom row shows the model components: (d) the PSF, (e) the host galaxy (modeled by a single Sérsic component with index $n \approx 1.66$), and (f) the neighboring galaxies. Images are on a logarithmic scale and are 0.77' \times 0.54' in angular size. The χ^2_ν value of the model fit is reported above the images. We observe a slight artifact of an imperfect PSF which resulted in a higher χ^2_ν , but the majority of the flux is well accounted for by the model.

GALFIT advisory document⁴. This adjustment, however, resulted in an incorrect magnitude parameter with an offset (the rest of the parameters remain consistent). The magnitudes reported in Table 2 have been corrected for this offset and are quoted accurately.

We determined the NIR AGN position to be the PSF position in the ‘best-fit’ GALFIT model (labeled as

PSF/AGN in Table 2). We calculated the positional uncertainty of the NIR AGN by summing in quadrature the 1 σ uncertainty of the GALFIT model, 1 σ RMS of the right ascension, and 1 σ RMS of the declination of the Gaia-aligned F160W image. The uncertainties in the Gaia-alignment were taken from FITS file headers of the F160W images (FITS header keywords RMS_RA and RMS_DEC) and are automatically generated by the HST pipeline for Gaia-aligned SVM products.

⁴ <https://users.obs.carnegiescience.edu/peng/work/galfit/advisory.html>

J1223+5409 ($\chi^2_\nu = 2.041$)

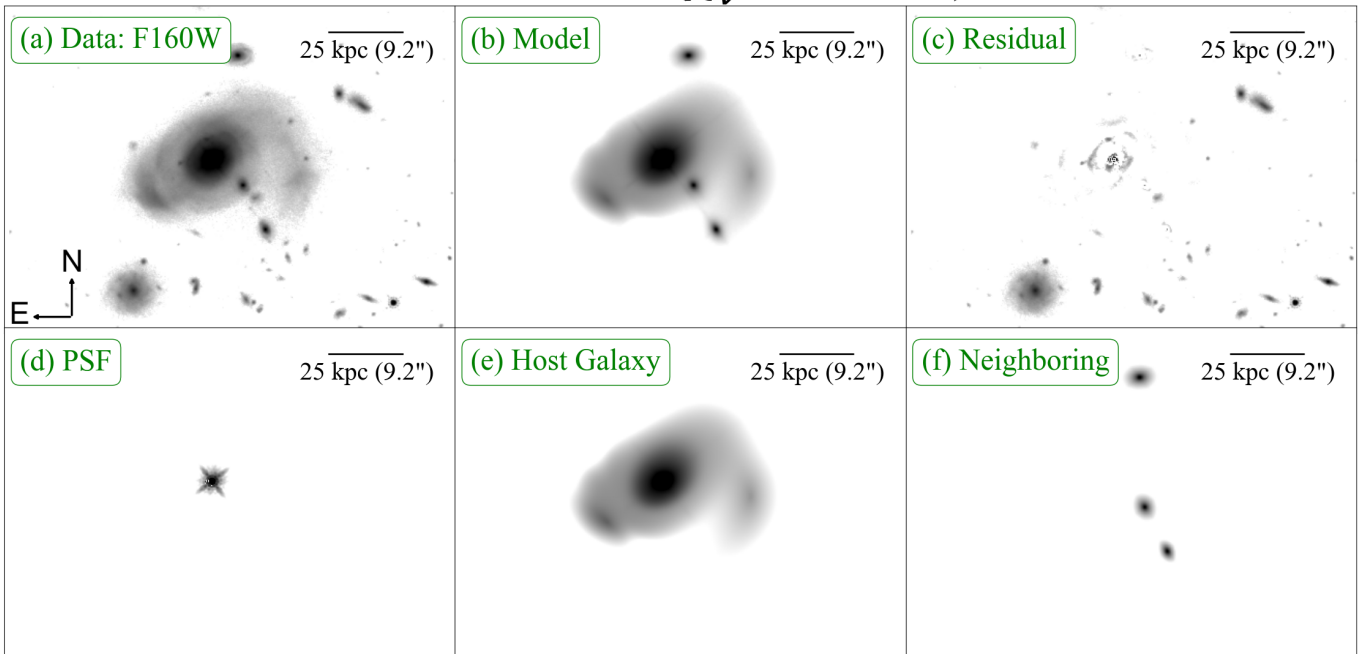


Figure 3. Best-fit GALFIT model of J1223+5409. Top row shows (a) the original image, (b) the model, and (c) the residual image. The bottom row shows the model components: (d) the PSF, (e) the host galaxy (modeled by four Sérsic components), and (f) the companion galaxies. Images are on a logarithmic scale and are $0.93' \times 0.67'$ in angular size. The χ^2_ν value of the model fit is reported above the images.

For J0948+6848 and J1223+5409, these values were ~ 8 mas and ~ 14 mas for right ascension and ~ 16 mas and ~ 8 mas for declination, respectively. The GALFIT contribution to the astrometric uncertainty was minimal, with the outputted PSF positional uncertainty being < 0.01 pixels (< 1.28 mas). Combining these contributions, the positional uncertainties of the NIR AGNs are ~ 18 mas (J0948+6848) and ~ 16 mas (J1223+5409).

4.2. Radio properties of the AGN

Figure 4 shows the 1.5 GHz continuum images of J0948+6848 and J1223+5409. Both systems have two compact radio continuum sources. We extracted the coordinate positions and radio properties of these detections using the Common Astronomy Software Application's (CASA's) two-dimensional Gaussian fitting tool IMFIT (CASA Team et al. 2022). From the derived source sizes and integrated flux densities, we also measured the brightness temperatures of each compact source using the prescription (Condon 1992; Pérez-Torres et al. 2021),

$$T_b = (1+z) \left(\frac{S_\nu}{\Omega} \right) \frac{c^2}{2kv^2} \\ \simeq 1.6 \times 10^3 (1+z) \left(\frac{S_\nu}{\text{mJy}} \right) \left(\frac{\nu}{\text{GHz}} \right)^{-2} \left(\frac{\theta_M \theta_m}{\text{arcsec}^2} \right)^{-1} \text{ K}, \quad (3)$$

where c is the speed of light, k is the Boltzmann constant, S_ν is the source flux density measured at frequency ν , and $\Omega = \pi \theta_M \theta_m / (4 \ln 2)$ is the solid angle subtended by the source assuming an elliptical Gaussian morphology, with θ_M and θ_m corresponding to the FWHM of the deconvolved major and minor axes of the fitted Gaussian, respectively. The factor of $(1+z)$ was added to account for the redshift of the source. For unresolved detections, we report brightness temperatures as lower-limits based on the upper-limits on the deconvolved source size. The derived properties are presented in Table 3. The listed coordinates have an astrometric uncertainty of up to ~ 10 mas (Fomalont et al. 1999), based on the milliarcsecond-scale positional shifts observed by previous VLBA L-band observations using a single phase-referencing calibrator separated by a few degrees from the target (e.g., Fomalont et al. 1999; Wrobel et al. 2004). The positional uncertainty of the phase

Table 2. GALFIT ‘best fit’ model parameters of host galaxies

(1) Source	(2) Comp.	(3) R.A. (J2000)	(4) Dec. (J2000)	(5) Mag	(6) R_e (‘)	(7) n	(8) Axis Ratio	(9) θ (deg)	(10) Fourier (m : (a_m, ϕ_m))	(11) Bending (m : a_m)
J0948+6848	PSF/AGN	09:48:22.463	+68:48:35.235	16.45						
		09:48:22.462	+68:48:35.228	16.54	2.31	1.66	0.73	29.89		
J1223+5409	PSF/AGN	12:23:13.217	+54:09:06.418	17.34						
		Sérsic	12:23:13.215	+54:09:06.445	16.75	0.63	1.86	0.80	-66.49	
Sérsic		12:23:13.316	+54:09:05.307	16.78	2.03	0.36	0.82	-54.68	1: (0.79, 30.72)	
		Sérsic	12:23:11.952	+54:09:04.175	17.98	9.89	1.38	0.46	0.81	1: (-0.24, -100.40)
Sérsic		12:23:14.098	+54:09:01.733	17.00	2.53	0.40	0.94	47.51	1: (0.79, -103.26)	2: 35.4
		Sérsic								1: -4.96; 2: 0.85

NOTE—Column (1): Source name. Column (2): GALFIT model component. Column (3): Right ascension. The positional uncertainties in right ascension are ~ 8 mas and ~ 14 mas for J0948+6858 and J1223+5409, respectively. Column (4): Declination. The positional uncertainty in declination are ~ 16 mas and ~ 8 mas for J0948+6858 and J1223+5409, respectively. The positional uncertainties for Columns (3) and (4) were calculated via a quadrature sum of the 1σ error outputted by the GALFIT model and 1σ error of the Gaia-alignment performed on the HST image. Column (5): Integrated magnitude in the AB system, following the standard definition $m_{tot} = -2.5 \log_{10}(F_\nu) - 48.60$ for a flux density F_ν . Column (6): Effective radius in arcseconds. Column (7): Sérsic index. Column (8): Ratio of major axis and minor axis. Column (9): Position angle. Column (10): Azimuthal fourier mode, amplitude, and phase angle. Phase angles are reported in degrees. Column (11): Bending mode and amplitude. Note that two different bending modes were used for the one of the Sérsic components for J1223+5409.

calibrator, switching angle errors, and atmospheric variations are likely contributing to these errors.

All four detections have high brightness temperatures ($T_b \sim 10^8 - 10^{10}$ K) that are consistent with non-thermal synchrotron-dominated emission driven by AGN activity ($> 10^5$ K; e.g., Condon et al. 1991; Condon 1992). We tentatively interpret the peaks of the radio emission in both target images as the positions of the radio AGN cores. In Section 5.2, however, we discuss the possible origins of the secondary detections.

4.3. Radio-Near Infrared AGN offsets

Here, we compare the NIR AGN position (Table 2) and the radio AGN position (Table 3). We sum in quadrature the positional uncertainties of the NIR AGN positions (~ 18 mas and ~ 16 mas for J0948+6848 and J1223+5409, respectively) and the VLBA positional uncertainty (~ 10 mas) to calculate 1σ relative astrometric uncertainties of ~ 20 mas and ~ 19 mas, respectively. We find that the projected spatial offsets are $< 2\sigma$ for J0948+6848 and $< 3\sigma$ for J1223+5409, and are thus insignificant. This places a 3σ upper-limit of < 268 pc ($< 0.08''$) and < 297 pc ($< 0.11''$) (calculated by summing the measured projected offset and the 3σ relative astrometric uncertainties), respectively, for the projected spatial offset between the radio AGN and NIR AGN if the systems host ‘radio-NIR’ dual AGN similar to CXO J101527.2+625911 (Kim et al. 2019). We tentatively conclude that the radio-detected and NIR-detected AGN are spatially coincident.

We also compare the AGN positions to the optical nucleus of each system (marked as a white star in Figure 4), as reported in the Gaia Data Release 3 catalog (Gaia Collaboration et al. 2023). We find that the Gaia positions are within the 3σ astrometric uncertainty of both the NIR and radio AGN positions. We therefore deduce a tentative positional agreement between the optical, NIR, and radio detections, despite the higher rates of error in Gaia’s astrometric solutions for extended host galaxies, particularly at lower red-shift (Hwang et al. 2020).

5. DISCUSSION

While we cannot confirm the presence of a ‘radio-NIR’ dual AGN in our pilot sample, the detection of two high brightness temperature ($> 10^8$ K; Table 3) radio continuum detections in both systems suggest two possible scenarios: a dual radio AGN scenario and a radio core-jet scenario. Since our single radio band observations are insufficient to derive a precise spectral index to distinguish between flat-spectrum AGN cores (e.g., Nagar et al. 2000) and steep-spectrum radio jets (e.g., Hov-

atta et al. 2014), we instead utilize archival data sets to consider each case.

5.1. Dual/Binary AGN scenario

In a dual/binary AGN scenario, the pairs of radio detections would represent two distinct AGN cores with projected nuclear separations of ~ 90 pc and ~ 56 pc for J0948+6848 and J1223+5409, respectively. These projected nuclear separations are comparable to those estimated for the candidate dual/binary AGN identified based on Gaia-VLBA offsets by Chen et al. (2023). At these projected separations, the SMBH pair is likely gravitationally bound and is expected to be in the stellar hardening phase of the SMBH merger in which the SMBH pair sheds energy primarily via stellar three-body interactions (Koss et al. 2023).

For each system, we estimate the projected velocity difference of the co-orbiting SMBHs from the spectral decomposition of the double-peaked [OIII] lines reported by Kim et al. (2020) (278 km s $^{-1}$ and 232 km s $^{-1}$ for J0948+6848 and J1223+5409, respectively). Assuming a Keplerian orbit, the sum of the two SMBH masses would be $\log(M_{\text{BH, total}}/M_{\odot}) \sim 9.2$ and 8.8, respectively. Dual AGN with SMBH masses of similar orders of magnitude have been detected (e.g., $\log(M_{\text{BH, total}}/M_{\odot}) \sim 8.6$ for UGC 4211; Koss et al. 2023), making this a plausible scenario.

We note, however, that this calculation assumes two distinct NLRs, each associated with a SMBH. Indeed, in a previous study, only $\sim 2\%$ of double-peaked [OIII] lines are attributed to dual/binary AGN with separate NLRs (Fu et al. 2012). Since the [OIII] emission discussed here is not spatially resolved to the parsec-scales probed by the VLBA, we cannot prove nor disprove this scenario.

5.2. Core-Jet scenario

Alternatively, it is also possible that our VLBA detections are tracing clumpy emission from a radio jet. As determined from the relative positions of the two compact VLBA detections, such a core-jet structure would have a position angle of ~ 10 degrees and ~ 91 degrees for J0948+6848 and J1223+5409, respectively (rotating east where north is 0 degrees).

For J1223+5409, this appears to conflict with the position angle of the potential radio jet detected at lower resolutions. For example, Jarvis et al. (2021) conducted multi-frequency (1.4 GHz and 5 GHz) radio observations of J1223+5409 at $\sim 0.3''$ resolution (~ 800 parsecs) using the Very Large Array (VLA). They constrained a spectral index of approximately $\alpha_{1.4}^{5.0} = -0.5 \pm 0.3$ for the core (assuming $S_{\nu} \propto \nu^{\alpha}$ where S_{ν} is the flux density at frequency ν), which they tentatively report as evidence of an AGN with an active radio jet. Both these

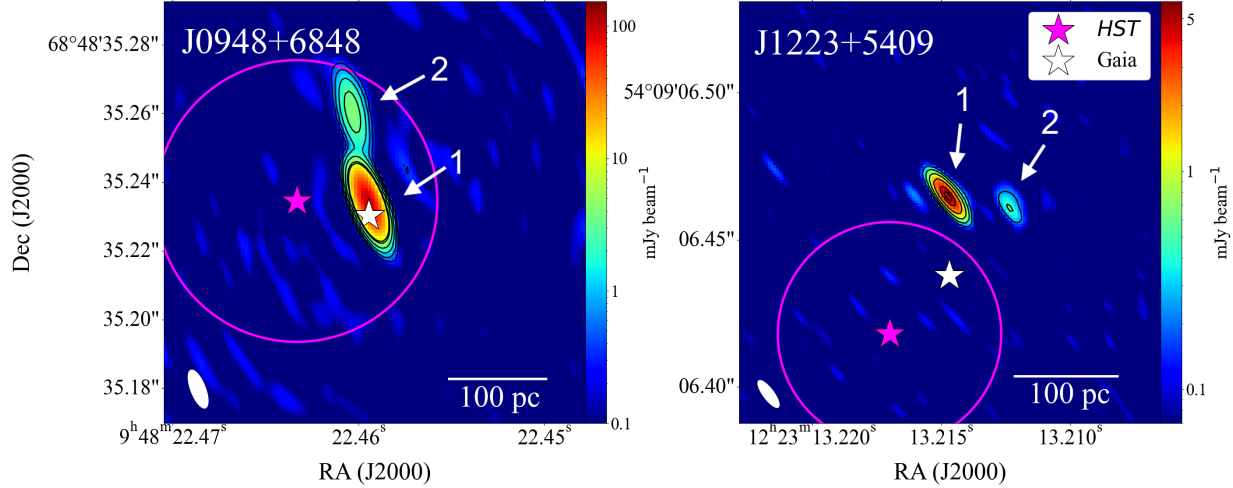


Figure 4. VLBA continuum images at 1.5 GHz for J0948+6848 (left) and J1223+5409 (right) on a logarithmic color scale. Black contours show 5σ , 10σ , 20σ , 40σ , 80σ , 100σ levels. Detections are labeled as components 1 and 2 in each system. The magenta stars indicate the GALFIT-determined position of the NIR-detected AGN, with the magenta circle representing the 2σ relative astrometric uncertainty of the *HST* and VLBA images. The white star is the Gaia-defined position of the host galaxy's nucleus with an uncertainty approximately consistent with the magenta circle. The synthesized beam sizes are shown in the bottom left as white filled ellipses. We do not observe a significant ($> 3\sigma$) spatial offset between the NIR-detected AGN and the radio-detected AGN.

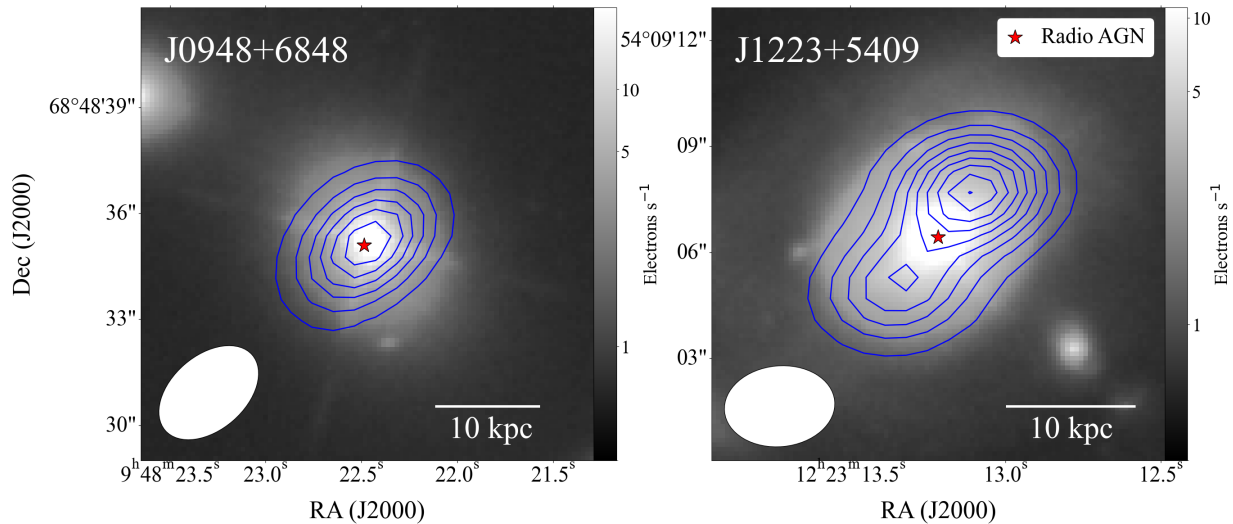


Figure 5. Greyscale WFC3/IR F160W images of J0948+6848 (left) and J1223+5409 (right) on a logarithmic scale. Images are oriented such that north is up and east is to the left and are $\sim 0.21' \times 0.21'$ in angular size. The red star is the position of the brightest VLBA-detected radio source, though the position of the secondary source also falls within the area of the star. VLASS 3 GHz radio contours are overlaid in blue, showing 100σ levels (100σ , 200σ , 300σ ...) where the 1σ RMS is $\sim 120\mu\text{Jy beam}^{-1}$. The synthesized radio beam is shown as a white ellipse in the bottom left. For both systems, the VLBA-detected AGN cores and NIR center are relatively spatially coincident. The VLASS radio peak of J1223+5409, however, is offset by kiloparsec-scales.

Table 3. Gaussian-fitted Radio Properties at 1.5 GHz

(1) Source	(2) Comp.	(3) R.A. (J2000)	(4) Dec. (J2000)	(5) θ_M (mas)	(6) θ_m (mas)	(7) S_ν (mJy)	(8) Peak Flux (mJy beam $^{-1}$)	(9) T_b (K)
J0948+6848	1	09:48:22.460	+68:48:35.234	3.0 \pm 0.1	0.55 \pm 0.06	106.7 \pm 11	102.3 \pm 10 (1894 σ)	(5.4 \pm 0.8) \times 10 ¹⁰
	2	09:48:22.460	+68:48:35.258	19.6 \pm 3.3	1.6 \pm 1.1	9.2 \pm 1.3	3.9 \pm 0.6 (72 σ)	(2.5 \pm 1.8) \times 10 ⁸
J1223+5409	1	12:23:13.215	+54:09:06.465	< 2.0*	< 0.94*	5.1 \pm 0.5	5.0 \pm 0.5 (111 σ)	\geq 2.2 \times 10 ⁹
	2	12:23:13.212	+54:09:06.461	< 2.0*	< 0.94*	0.7 \pm 0.1	0.45 \pm 0.06 (10 σ)	\geq 3.1 \times 10 ⁸

*Upper-limits on the deconvolved source size due to unresolved point source.

NOTE—Column (1): Source name. Column (2): Component number as labeled in Figure 4. Column (3): Right ascension of the detection. Column (4): Declination of the detection. For the coordinate positions in columns (3) and (4), the astrometric uncertainty is \sim 10 mas. Columns (5) and (6): FWHM of the major and minor axes of the radio detection, deconvolved from the synthesized beam. Column (7): Integrated flux density at 1.5 GHz (18 cm). Column (8): Peak flux density at 1.5 GHz (18 cm). The sigma levels in parentheses refer to the significance of the measured flux density with respect to the 1σ RMS noise of the image. Column (9): Redshift-corrected brightness temperature. The 1σ uncertainties listed for Columns (5) through Column (9) are based on the estimated flux calibration uncertainty (\sim 10%) and/or the IMFIT parameter uncertainties.

VLA observations by [Jarvis et al. \(2021\)](#) (see their Figure 4) and the lower resolution 3 GHz VLASS images of J1223+5409 (see blue contours on the right panel of Figure 5) reveal a bipolar emission structure extending from the central core, possibly tracing a large-scale radio jet. From the VLASS image, we estimate that the structure is elongated along an axis with a 21 degree position angle. Given the difference of ~ 70 degrees compared to the VLBA-determined position angle, this suggests that, in a core-jet scenario, the kiloparsec-scale jet structure has a drastically different orientation than the parsec-scale jet emission.

Table 4. VLASS Flux Densities at 3 GHz

(1) Source	(2) Date	(3) $S_{3\text{GHz}}$ (Jy)
J0948+6848	Oct. 21, 2017	0.090 ± 0.009
	Sep. 01, 2020	0.106 ± 0.003
	Feb. 15, 2023	0.105 ± 0.003
J1223+5409	Nov. 17, 2017	0.181 ± 0.019
	Aug. 20, 2020	0.204 ± 0.006
	Feb. 7, 2023	0.200 ± 0.006

NOTE—Column (1): Source name. Column (2): Date of VLASS observations. Column (3): Total flux density at 3 GHz, measured over a circular aperture with a $20''$ radius. The reported uncertainty considers 1σ RMS of the image and total flux density uncertainty of VLASS ($\sim 10\%$ for epoch 1.1, and $\sim 3\%$ for the remaining epochs).

Similar systems have been observed with different radio jet trajectories at parsec-scales compared to kiloparsec-scales (e.g., [Beswick et al. 2004](#)), pointing to the possibility of extreme jet axis precession and/or the formation of a new radio jet in these systems. Newborn radio jets, however, are expected to generate high flux variability over year to decade timescales (100–2500%, [Nyland et al. 2020](#); [Wołowska et al. 2021](#); [Zhang et al. 2022](#)). We searched for evidence of this flux variability by comparing VLASS 3 GHz continuum images across the three observing epochs. To maximize image quality, we utilized the publicly-available calibrated measurement sets and performed self-calibration on both the phase calibrator and the final target using the customized VLASS Single Epoch Continuum Pipeline ([Carlson et al. 2022](#)). Extracting flux densities using a circular aperture with a $20''$ radius, we measured only

a ~ 10 –15% flux density increase over the three observing epochs in both systems (Table 4). Although this is tentatively greater than the estimated flux density uncertainty of the calibrated images ($\sim 3\%$ ⁵), the measured flux density change could be a product of the antenna position error during the first epoch of VLASS that led to systematically low total flux density measurements (differences as high as 10%; [Gordon et al. 2021](#)). It is therefore unclear whether this flux density difference is physically meaningful.

Future matched-resolution multi-band radio observations will allow us to constrain spectral indices for each detection and differentiate between these two scenarios. Follow-up study, however, is warranted in either scenario given that these systems either (1) host some of the closest separation dual AGN detected thus far or (2) have experienced a sudden reorientation of the AGN jet-axis due to merger-driven dynamics (e.g., [Roos 1988](#); [Abraham 2018](#)) or accretion instabilities (e.g., [Liska et al. 2018](#); [Lalakos et al. 2022](#)).

6. CONCLUSION

Using high-resolution NIR and radio images from the *HST* and the VLBA, we searched for AGN pairs in two local ($z < 0.25$) candidate dual AGN ([Kim et al. 2020](#)). From the NIR images, we modeled the galaxies’ structure to constrain the NIR AGN position. From the radio continuum images, we performed two-dimensional Gaussian fitting to extract the source position and radio properties. Our results are as follows:

- In both targets, we do not find significant spatial offsets between the NIR-detected AGN and the radio-detected AGN. If the AGN observed at each wavelength are distinct, then their projected nuclear separation must be <268 pc ($<0.08''$) and <297 pc ($<0.11''$) for J0948+6848 and J1223+5409, respectively.
- We detected two compact radio sources in both J0948+6848 and J1223+5409 that have brightness temperatures consistent with AGN activity ($> 10^7$ K). The galaxies host either a pair of radio AGN cores or a core-jet system with clumpy emission from a radio jet. Future matched-resolution multi-band radio observations are necessary to distinguish between these scenarios.

⁵ https://library.nrao.edu/public/memos/vla/vlass_VLASS_013.pdf

ACKNOWLEDGMENTS

The National Radio Astronomy Observatory is a facility of the National Science Foundation operated under cooperative agreement by Associated Universities, Inc. This research is based on observations made with the NASA/ESA Hubble Space Telescope obtained from the Space Telescope Science Institute, which is operated by the Association of Universities for Research in Astronomy, Inc., under NASA contract NAS 5-26555. These observations are associated with program HST-GO-16485. MAJ acknowledges support from grant HST-GO-16485.001-A. This work made use of the Swinburne University of Technology software correlator, developed as part of the Australian Major National Re-

search Facilities Programme and operated under license. MK was supported by the National Research Foundation of Korea (NRF) grant funded by the Korean government (MSIT) (Nos. RS-2024-00347548 and RS-2025-16066624). JHK acknowledges the support from the National Research Foundation of Korea (NRF) grants, No. 2021M3F7A1084525 and No. 2020R1A2C3011091, and the Institute of Information & Communications Technology Planning & Evaluation (IITP) grant, No. RS-2021-II212068 funded by the Korean government (MSIT). EG acknowledges the generous support of the Cottrell Scholar Award through the Research Corporation for Science Advancement. EG is grateful to the Mittelman Family Foundation for their generous support.

REFERENCES

Abraham, Z. 2018, *Nature Astronomy*, 2, 443, doi: [10.1038/s41550-018-0484-2](https://doi.org/10.1038/s41550-018-0484-2)

Agazie, G., Anumarlapudi, A., Archibald, A. M., et al. 2023a, *ApJL*, 951, L8, doi: [10.3847/2041-8213/acdac6](https://doi.org/10.3847/2041-8213/acdac6)

—. 2023b, *ApJL*, 952, L37, doi: [10.3847/2041-8213/ace18b](https://doi.org/10.3847/2041-8213/ace18b)

Assef, R. J., Stern, D., Kochanek, C. S., et al. 2013, *ApJ*, 772, 26, doi: [10.1088/0004-637X/772/1/26](https://doi.org/10.1088/0004-637X/772/1/26)

Berczik, P., Arca Sedda, M., Sobolenko, M., et al. 2022, *A&A*, 665, A86, doi: [10.1051/0004-6361/202244354](https://doi.org/10.1051/0004-6361/202244354)

Beswick, R. J., Peck, A. B., Taylor, G. B., & Giovannini, G. 2004, *MNRAS*, 352, 49, doi: [10.1111/j.1365-2966.2004.07892.x](https://doi.org/10.1111/j.1365-2966.2004.07892.x)

Blecha, L., Snyder, G. F., Satyapal, S., & Ellison, S. L. 2018, *MNRAS*, 478, 3056, doi: [10.1093/mnras/sty1274](https://doi.org/10.1093/mnras/sty1274)

Burke-Spolaor, S. 2011, *MNRAS*, 410, 2113, doi: [10.1111/j.1365-2966.2010.17586.x](https://doi.org/10.1111/j.1365-2966.2010.17586.x)

Carlson, E., Kimball, A., & Patil, P. 2022, User-Defined Imaging of the Very Large Array Sky Survey, 1, doi: [10.5281/zenodo.7076243](https://doi.org/10.5281/zenodo.7076243)

CASA Team, Bean, B., Bhatnagar, S., et al. 2022, *PASP*, 134, 114501, doi: [10.1088/1538-3873/ac9642](https://doi.org/10.1088/1538-3873/ac9642)

Chandrasekhar, S. 1943, *ApJ*, 97, 255, doi: [10.1086/144517](https://doi.org/10.1086/144517)

Chen, Y.-C., Liu, X., Lazio, J., et al. 2023, *ApJ*, 958, 29, doi: [10.3847/1538-4357/ad00b3](https://doi.org/10.3847/1538-4357/ad00b3)

Ciurlo, A., Mannucci, F., Yeh, S., et al. 2023, *A&A*, 671, L4, doi: [10.1051/0004-6361/202345853](https://doi.org/10.1051/0004-6361/202345853)

Clark, B. G. 1980, *A&A*, 89, 377

Condon, J. J. 1992, *ARA&A*, 30, 575, doi: [10.1146/annurev.aa.30.090192.0003043](https://doi.org/10.1146/annurev.aa.30.090192.0003043)

Condon, J. J., Huang, Z.-P., Yin, Q. F., & Thuan, T. X. 1991, *ApJ*, 378, 65, doi: [10.1086/170407](https://doi.org/10.1086/170407)

De Rosa, A., Vignali, C., Bogdanović, T., et al. 2019, *NewAR*, 86, 101525, doi: [10.1016/j.newar.2020.101525](https://doi.org/10.1016/j.newar.2020.101525)

Deller, A. T., Brisken, W. F., Phillips, C. J., et al. 2011, *PASP*, 123, 275, doi: [10.1086/658907](https://doi.org/10.1086/658907)

Euclid Collaboration, La Marca, A., Wang, L., et al. 2025, arXiv e-prints, arXiv:2503.15317, doi: [10.48550/arXiv.2503.15317](https://doi.org/10.48550/arXiv.2503.15317)

Fabbiano, G., Wang, J., Elvis, M., & Risaliti, G. 2011, *Nature*, 477, 431, doi: [10.1038/nature10364](https://doi.org/10.1038/nature10364)

Fomalont, E. B., Goss, W. M., Beasley, A. J., & Chatterjee, S. 1999, *AJ*, 117, 3025, doi: [10.1086/300877](https://doi.org/10.1086/300877)

Fu, H., Yan, L., Myers, A. D., et al. 2012, *ApJ*, 745, 67, doi: [10.1088/0004-637X/745/1/67](https://doi.org/10.1088/0004-637X/745/1/67)

Gaia Collaboration, Vallenari, A., Brown, A. G. A., et al. 2023, *A&A*, 674, A1, doi: [10.1051/0004-6361/202243940](https://doi.org/10.1051/0004-6361/202243940)

Glikman, E., Simmons, B., Mailly, M., et al. 2015, *ApJ*, 806, 218, doi: [10.1088/0004-637X/806/2/218](https://doi.org/10.1088/0004-637X/806/2/218)

Glikman, E., Langgin, R., Johnstone, M. A., et al. 2023, *ApJL*, 951, L18, doi: [10.3847/2041-8213/acda2f](https://doi.org/10.3847/2041-8213/acda2f)

Gordon, Y. A., Boyce, M. M., O'Dea, C. P., et al. 2021, *ApJS*, 255, 30, doi: [10.3847/1538-4365/ac05c0](https://doi.org/10.3847/1538-4365/ac05c0)

Greene, J. E., & Ho, L. C. 2005, *ApJ*, 627, 721, doi: [10.1086/430590](https://doi.org/10.1086/430590)

Greisen, E. W. 2003, in *Astrophysics and Space Science Library*, Vol. 285, *Information Handling in Astronomy - Historical Vistas*, ed. A. Heck, 109, doi: [10.1007/0-306-48080-8_7](https://doi.org/10.1007/0-306-48080-8_7)

Gross, A. C., Chen, Y.-C., Oguri, M., et al. 2025, *ApJ*, 989, 112, doi: [10.3847/1538-4357/ade671](https://doi.org/10.3847/1538-4357/ade671)

Hildebrand, R. H. 1983, *QJRAS*, 24, 267

Hopkins, P. F., Hernquist, L., Cox, T. J., et al. 2006, *ApJS*, 163, 1, doi: [10.1086/499298](https://doi.org/10.1086/499298)

Hovatta, T., Aller, M. F., Aller, H. D., et al. 2014, AJ, 147, 143, doi: [10.1088/0004-6256/147/6/143](https://doi.org/10.1088/0004-6256/147/6/143)

Hwang, H.-C., Shen, Y., Zakamska, N., & Liu, X. 2020, ApJ, 888, 73, doi: [10.3847/1538-4357/ab5c1a](https://doi.org/10.3847/1538-4357/ab5c1a)

Izquierdo-Villalba, D., Sesana, A., Bonoli, S., & Colpi, M. 2022, MNRAS, 509, 3488, doi: [10.1093/mnras/stab3239](https://doi.org/10.1093/mnras/stab3239)

Jarvis, M. E., Harrison, C. M., Mainieri, V., et al. 2021, MNRAS, 503, 1780, doi: [10.1093/mnras/stab549](https://doi.org/10.1093/mnras/stab549)

Just, A., Khan, F. M., Berczik, P., Ernst, A., & Spurzem, R. 2011, MNRAS, 411, 653, doi: [10.1111/j.1365-2966.2010.17711.x](https://doi.org/10.1111/j.1365-2966.2010.17711.x)

Kellermann, K. I., Condon, J. J., Kimball, A. E., Perley, R. A., & Ivezić, Ž. 2016, ApJ, 831, 168, doi: [10.3847/0004-637X/831/2/168](https://doi.org/10.3847/0004-637X/831/2/168)

Kim, D. C., Yoon, I., Evans, A. S., et al. 2020, ApJ, 904, 23, doi: [10.3847/1538-4357/abb9a0](https://doi.org/10.3847/1538-4357/abb9a0)

Kim, D. C., Yoon, I., Privon, G. C., et al. 2017, ApJ, 840, 71, doi: [10.3847/1538-4357/aa6030](https://doi.org/10.3847/1538-4357/aa6030)

Kim, D. C., Momjian, E., Yoon, I., et al. 2019, ApJ, 882, 149, doi: [10.3847/1538-4357/ab2e0b](https://doi.org/10.3847/1538-4357/ab2e0b)

Kollatschny, W., Weilbacher, P. M., Ochmann, M. W., et al. 2020, A&A, 633, A79, doi: [10.1051/0004-6361/201936540](https://doi.org/10.1051/0004-6361/201936540)

Koss, M. J., Blecha, L., Bernhard, P., et al. 2018, Nature, 563, 214, doi: [10.1038/s41586-018-0652-7](https://doi.org/10.1038/s41586-018-0652-7)

Koss, M. J., Treister, E., Kakkad, D., et al. 2023, ApJL, 942, L24, doi: [10.3847/2041-8213/aca8f0](https://doi.org/10.3847/2041-8213/aca8f0)

Lacy, M., Storrie-Lombardi, L. J., Sajina, A., et al. 2004, ApJS, 154, 166, doi: [10.1086/422816](https://doi.org/10.1086/422816)

Lalakos, A., Gottlieb, O., Kaaz, N., et al. 2022, ApJL, 936, L5, doi: [10.3847/2041-8213/ac7bed](https://doi.org/10.3847/2041-8213/ac7bed)

Liska, M., Hesp, C., Tchekhovskoy, A., et al. 2018, MNRAS, 474, L81, doi: [10.1093/mnrasl/slx174](https://doi.org/10.1093/mnrasl/slx174)

Mannucci, F., Pancino, E., Belfiore, F., et al. 2022, Nature Astronomy, 6, 1185, doi: [10.1038/s41550-022-01761-5](https://doi.org/10.1038/s41550-022-01761-5)

Müller-Sánchez, F., Comerford, J. M., Nevin, R., et al. 2015, ApJ, 813, 103, doi: [10.1088/0004-637X/813/2/103](https://doi.org/10.1088/0004-637X/813/2/103)

Nagar, N. M., Falcke, H., Wilson, A. S., & Ho, L. C. 2000, ApJ, 542, 186, doi: [10.1086/309524](https://doi.org/10.1086/309524)

Nyland, K., Dong, D. Z., Patil, P., et al. 2020, ApJ, 905, 74, doi: [10.3847/1538-4357/abc341](https://doi.org/10.3847/1538-4357/abc341)

Orosz, G., & Frey, S. 2013, A&A, 553, A13, doi: [10.1051/0004-6361/201321279](https://doi.org/10.1051/0004-6361/201321279)

Peng, C. Y., Ho, L. C., Impey, C. D., & Rix, H.-W. 2010, AJ, 139, 2097, doi: [10.1088/0004-6256/139/6/2097](https://doi.org/10.1088/0004-6256/139/6/2097)

Pérez-Torres, M., Mattila, S., Alonso-Herrero, A., Aalto, S., & Efstathiou, A. 2021, A&A Rv, 29, 2, doi: [10.1007/s00159-020-00128-x](https://doi.org/10.1007/s00159-020-00128-x)

Pfeifle, R. W., Weaver, K. A., Secrest, N. J., Rothberg, B., & Patton, D. R. 2025, ApJS, 281, 25, doi: [10.3847/1538-4365/adf845](https://doi.org/10.3847/1538-4365/adf845)

Popkov, A. V., Kovalev, Y. Y., Plavin, A. V., Petrov, L. Y., & Pashchenko, I. N. 2025, MNRAS, 543, 479, doi: [10.1093/mnras/staf1480](https://doi.org/10.1093/mnras/staf1480)

Rafikov, R. R. 2016, ApJ, 827, 111, doi: [10.3847/0004-637X/827/2/111](https://doi.org/10.3847/0004-637X/827/2/111)

Reardon, D. J., Zic, A., Shannon, R. M., et al. 2023, ApJL, 951, L6, doi: [10.3847/2041-8213/acdd02](https://doi.org/10.3847/2041-8213/acdd02)

Ricci, C., Bauer, F. E., Treister, E., et al. 2017, MNRAS, 468, 1273, doi: [10.1093/mnras/stx173](https://doi.org/10.1093/mnras/stx173)

Ricci, C., Privon, G. C., Pfeifle, R. W., et al. 2021, MNRAS, 506, 5935, doi: [10.1093/mnras/stab2052](https://doi.org/10.1093/mnras/stab2052)

Rodriguez, C., Taylor, G. B., Zavala, R. T., et al. 2006, ApJ, 646, 49, doi: [10.1086/504825](https://doi.org/10.1086/504825)

Roos, N. 1988, ApJ, 334, 95, doi: [10.1086/166820](https://doi.org/10.1086/166820)

Rubinur, K., Das, M., & Kharb, P. 2019, MNRAS, 484, 4933, doi: [10.1093/mnras/stz334](https://doi.org/10.1093/mnras/stz334)

Satyapal, S., Secrest, N. J., McAlpine, W., et al. 2014, ApJ, 784, 113, doi: [10.1088/0004-637X/784/2/113](https://doi.org/10.1088/0004-637X/784/2/113)

Satyapal, S., Secrest, N. J., Ricci, C., et al. 2017, ApJ, 848, 126, doi: [10.3847/1538-4357/aa88ca](https://doi.org/10.3847/1538-4357/aa88ca)

Schneider, D. P., Richards, G. T., Hall, P. B., et al. 2010, AJ, 139, 2360, doi: [10.1088/0004-6256/139/6/2360](https://doi.org/10.1088/0004-6256/139/6/2360)

Schwartzman, E., Fudolig, P., Clarke, T. E., et al. 2025, ApJ, 987, 200, doi: [10.3847/1538-4357/add47c](https://doi.org/10.3847/1538-4357/add47c)

Shen, Y., Liu, X., Greene, J. E., & Strauss, M. A. 2011, ApJ, 735, 48, doi: [10.1088/0004-637X/735/1/48](https://doi.org/10.1088/0004-637X/735/1/48)

Smith, K. L., Shields, G. A., Bonning, E. W., et al. 2010, ApJ, 716, 866, doi: [10.1088/0004-637X/716/1/866](https://doi.org/10.1088/0004-637X/716/1/866)

Springel, V., White, S. D. M., Jenkins, A., et al. 2005, Nature, 435, 629, doi: [10.1038/nature03597](https://doi.org/10.1038/nature03597)

Steinborn, L. K., Dolag, K., Comerford, J. M., et al. 2016, MNRAS, 458, 1013, doi: [10.1093/mnras/stw316](https://doi.org/10.1093/mnras/stw316)

Treister, E., Schawinski, K., Urry, C. M., & Simmons, B. D. 2012, ApJL, 758, L39, doi: [10.1088/2041-8205/758/2/L39](https://doi.org/10.1088/2041-8205/758/2/L39)

Trindade Falcão, A., Turner, T. J., Kraemer, S. B., et al. 2024, ApJ, 972, 185, doi: [10.3847/1538-4357/ad6b91](https://doi.org/10.3847/1538-4357/ad6b91)

Urry, C. M., & Padovani, P. 1995, PASP, 107, 803, doi: [10.1086/133630](https://doi.org/10.1086/133630)

Van Wassenhove, S., Volonteri, M., Mayer, L., et al. 2012, ApJL, 748, L7, doi: [10.1088/2041-8205/748/1/L7](https://doi.org/10.1088/2041-8205/748/1/L7)

Veres, P. M., Gabányi, K. É., Frey, S., et al. 2021, ApJ, 922, 99, doi: [10.3847/1538-4357/ac307d](https://doi.org/10.3847/1538-4357/ac307d)

Volonteri, M., Dubois, Y., Pichon, C., & Devriendt, J. 2016, MNRAS, 460, 2979, doi: [10.1093/mnras/stw1123](https://doi.org/10.1093/mnras/stw1123)

Weigel, A. K., Schawinski, K., Treister, E., Trakhtenbrot, B., & Sanders, D. B. 2018, MNRAS, 476, 2308, doi: [10.1093/mnras/sty383](https://doi.org/10.1093/mnras/sty383)

Wołowska, A., Kunert-Bajraszewska, M., Mooley, K. P., et al. 2021, ApJ, 914, 22, doi: [10.3847/1538-4357/abe62d](https://doi.org/10.3847/1538-4357/abe62d)

Wrobel, J. M., Garrett, M. A., Condon, J. J., & Morganti, R. 2004, AJ, 128, 103, doi: [10.1086/421743](https://doi.org/10.1086/421743)

Xu, H., Chen, S., Guo, Y., et al. 2023, Research in Astronomy and Astrophysics, 23, 075024, doi: [10.1088/1674-4527/acdfa5](https://doi.org/10.1088/1674-4527/acdfa5)

Zhang, F., Shu, X., Sun, L., et al. 2022, ApJ, 938, 43, doi: [10.3847/1538-4357/ac8a9a](https://doi.org/10.3847/1538-4357/ac8a9a)